WILEY

Acute changes in histopathology and intravascular imaging after catheter-based renal denervation in a porcine model

Atsushi Sakaoka, MS[1,2] 🔟 | Akiyuki Takami, MS[3] | Yuji Onimura, MS[1] |

Hitomi Hagiwara, BS[1] | Hisako Terao, BS[1] | Fumiaki Kumagai[4] |

Kiyoshi Matsumura, PhD[2]

[1]R&D Headquarters, Terumo Corporation, Tokyo, Japan

[2]Graduate School of Engineering, Osaka Institute of Technology, Osaka, Japan

[3]Faculty of Medical Sciences, University of Fukui, Fukui, Japan

[4]Laboratory of Safety Evaluation, Division of Safety, Hatano Research Institute, Food and Drug Safety Center, Kanagawa, Japan

Correspondence
Atsushi Sakaoka MS, R&D Headquarters, Terumo Corporation 1500 Inokuchi, Nakai-machi, Ashigarakami-gun Kanagawa 259-0151, Japan.
Email: atsushi_sakaoka@terumo.co.jp

Funding information
This study was supported by Terumo Corporation, Tokyo, Japan.

Abstract

Objectives: We first aimed to identify the histopathological changes occurring immediately after renal denervation (RDN) with radiofrequency energy, and then to assess the feasibility of determining procedural success using currently available clinical intravascular imaging techniques.

Background: Catheter-based RDN has been used as an alternative therapy for hypertension. However, no practical endpoint to determine procedural success during treatment has been established.

Methods: A total of 39 ablation lesions were induced in vivo in eight porcine renal arteries and a total of 15 ablation lesions were induced ex vivo in five excised porcine renal arteries with a radiofrequency delivery device. Acute histological changes and appearance on intravascular imaging of the lesions were investigated with light microscopy, transmission electron microscopy, intravascular ultrasound (IVUS), and optical frequency domain imaging (OFDI).

Results: Marked changes were noted in media, adventitia, and perirenal-arterial nerves immediately after in vivo ablation. Changes visualized on IVUS were characterized by focal adventitial thickening comprising a relatively echogenic layer around a heterogeneously hypoechoic interior region, and on OFDI as disappearance of the external elastic membrane signals with high scattering of signals in the surface layer. The changes after ex vivo ablation were histopathologically identical to those from in vivo ablation. There were statistically significant positive correlations in measured dimensions (area, depth, width, and diameter) of ablation lesions between histopathology and IVUS/OFDI findings (Pearson correlation coefficients = 0.69–0.77).

Conclusions: These findings suggest that observation of treated renal arteries by IVUS or OFDI immediately after RDN improves the success rate of RDN.

KEYWORDS
intravascular ultrasound, optical coherence tomography, optical frequency domain imaging, pathology, radiofrequency, renal denervation

1 | INTRODUCTION

Hypertension is a well-known risk factor for cardiovascular and renal diseases [1]. As over-activity of sympathetic nerves around renal arteries contribute to hypertension [2], catheter-based renal denervation (RDN) to ablate renal sympathetic nerves has emerged as an
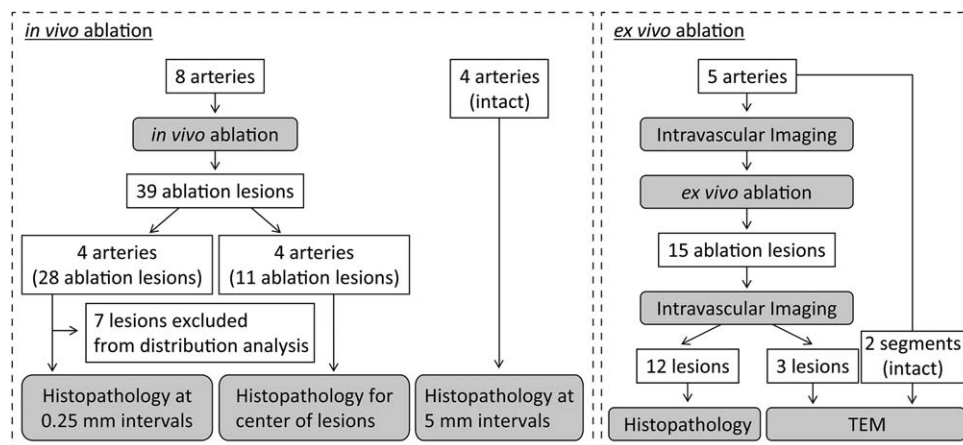
FIGURE 1 Flow diagram of the study

alternative therapy for hypertension. Among currently proposed technologies for RDN, radiofrequency is the standard treatment at present and its safety has been confirmed in many clinical trials [3–5]. The efficacy of RDN is, however, still controversial. Although early clinical trials demonstrated RDN with radiofrequency significantly reduced blood pressure [4,5], an initial sham-controlled and blinded clinical trial (the SYMPLICITY HTN-3 trial), failed to meet its efficacy endpoint [3]. It is suspected that inadequate RDN procedures by inexperienced physicians was a possible cause for the failure, but the challenging issue remains that no practical endpoint exists to determine procedural success immediately after the RDN procedure [6,7]. Although an ideal diagnostic technology is direct measurement of renal sympathetic activities during RDN procedures, there is no way to monitor sympathetic activities of internal organs in clinical settings [8].

Diagnostic technology for the procedural success during RDN procedures requires details of acute histopathological changes immediately after delivery of radiofrequency energy from an RDN device. Previous studies on histopathological changes after delivery of radiofrequency energy are almost limited to subacute (7 days) and chronic (90–180 days) time points, and hence detailed descriptions immediately after RDN treatment are lacking [9–11].

In this study, we ablated porcine renal arteries with a radiofrequency-delivering RDN device that has been used clinically [12,13], and investigated histopathological changes in detail with light microscopy and transmission electron microscopy (TEM). To explore the diagnostic feasibility of procedural success in RDN with intravascular imaging systems currently available in catheterization laboratories, we investigated whether an intravascular ultrasound (IVUS) and optical frequency domain imaging (OFDI), also referred to as optical coherence tomography (OCT), can detect radiofrequency-induced histopathological changes immediately after an RDN procedure.

2 | MATERIALS AND METHODS

2.1 | In vivo ablation

This study was conducted in accordance with the Guidelines for Proper Conduct of Animal Experiments (Science Council of Japan,

2006) and the protocol was approved by the Institutional Animal Care and Use Committee of R&D Headquarters at Terumo Corporation.

The study flow diagram is illustrated in Figure 1. A total of 39 ablation lesions were created in vivo in eight renal arteries (diameter: 5.37 ± 0.44 mm, range 4.94–6.28 mm) of five domestic swine (body weight: 63.9–76.9 kg) by delivery of 8 watts radiofrequency energy for 120 sec with a commercially available RDN system (Iberis; Terumo Corporation, Tokyo, Japan; Supporting Information Figure S1). All animals were euthanized under anesthesia immediately after ablation. Renal arteries were perfusion-fixed at 100 mm Hg with 10% neutral-buffered formalin. The harvested renal arteries were fixed in paraffin and stained with hematoxylin and eosin and Masson's trichrome with or without elastin staining. Among the eight renal arteries, four containing 28 ablation lesions were sectioned at approximately 0.25-mm intervals. Seven lesions among the 28 were excluded from distribution analysis as the lesions were not fully included in one histological block and thus transition of the lesions was incompletely captured. The remaining four renal arteries containing 11 ablation lesions were sectioned at the center of the lesions for histological examination. Histopathological changes by ablation were identified by comparison of the ablated arteries with four intact renal arteries from two untreated domestic swine.

The extent of lesions was assessed in histological sections with 0.25-mm intervals in a semiquantitative manner (Figure 3B,C). In each histological section, media was divided circumferentially into 12 equal regions (1–12 o'clock). The medial change was scored per region as: 0 = no change; 1 = nontransmural coagulation; 2 = transmural coagulation without medial thinning; 3 = transmural coagulation with medial thinning. Transmural coagulation was defined as coagulation of the full thickness of the affected media. To describe circumferential spread and depth of ablation, circumferential range and frequency of maximum score were calculated, respectively. Circumferential range (%) at each histological section was calculated as $100 \times$ (number of regions with a score ≥ 1)/12. The frequency of maximum score was calculated as the summation of the highest score at each histological section.
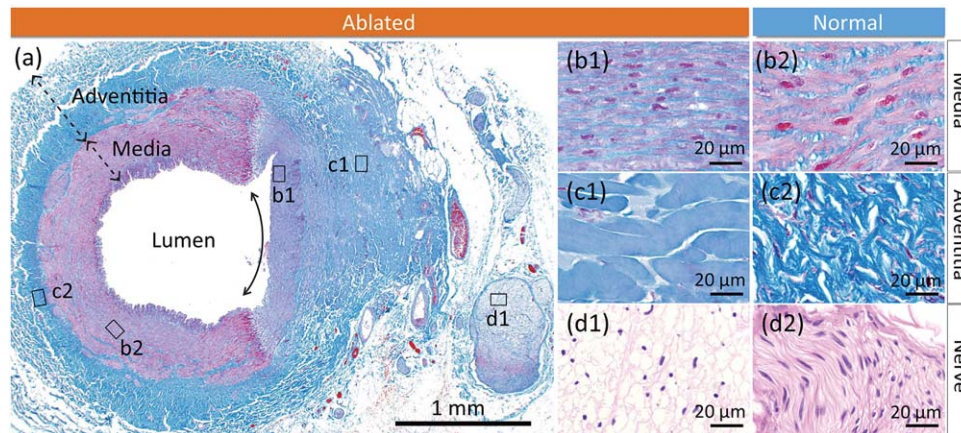
FIGURE 2 Representative histopathological images of the in vivo study with Masson's trichrome staining (a–c) and hematoxylin and eosin staining (d). Media appeared coagulated with a clear border (double arrow, a). Smooth muscle cells in ablated media showed atrophy and different staining properties (b1) compared with those in normal media (b2). Collagen fibers in ablated adventitia (c1) lost fibrous structures and swelled and hyalinized compared with those in normal adventitia (c2). Ablated nerves showed vacuolation and pyknosis (d1) compared with normal nerves in the same histological section outside the field of panel (a) (d2) [Color figure can be viewed at wileyonlinelibrary.com]

2.2 | Ex vivo ablation

Five renal arteries harvested from domestic swine were cut longitudinally and immersed in saline. The tip of the ablation catheter (Iberis) made contact with the arterial lumen and a total of 15 separate ablation lesions were created by delivery of 8 watts radiofrequency energy for 30–120 sec.

Intravascular cross sectional images of the 15 ablation lesions were acquired at pre- and post-ablation with an IVUS system (VISI-WAVE and ViewIT; Terumo Corporation; with a pullback speed of 1 or 2 mm/sec at a frame rate of 30 frames/sec) and an OFDI system (LUNAWAVE and FastView; Terumo Corporation; with a pullback speed of 5 mm/sec at a frame rate of 158 frames/sec). The 12 ablation lesions were fixed and processed for histopathology in the same way as in the in vivo study. The remaining three ablation lesions and two intact arterial segments were processed for TEM as follows. They were immersed in an ice-cold mixture of 0.1 mol/L phosphate buffered 2% paraformaldehyde and 1.25% glutaraldehyde overnight. Fixed tissues were postfixed in 0.1 mol/L phosphate buffered 2% osmium tetraoxide. After being dehydrated in serial ethanol solutions of graded concentrations, tissues were embedded in epoxy resin (Quetol-651; Nissin EM, Tokyo, Japan). Ultrathin sections were prepared from the center and edge of ablation lesions and intact segments. Sections were stained with uranyl acetate and lead citrate, and then observed under a transmission electron microscope (model HT7700; Hitachi, Tokyo, Japan). The diameter of collagen fibrils in ablated ($N = 30$) and intact adventitia ($N = 30$) in TEM images were measured with a computer-assisted image measurement system (ImageJ; NIH, Bethesda, MD, USA).

2.3 | Analysis of intravascular imaging

In IVUS analysis, the frame where the ablation lesion appeared maximal was selected per ablation lesion. Areas in adventitia, depths, and widths of ablation lesions were measured with an off-line computer-based software system (VISIATLAS; Terumo Corporation). In OFDI analysis, areas and depths of ablation lesions could not be measured as the deepest layer was invisible because of high signal attenuation. Widths of ablation lesions were not measured accurately either because of high signal attenuation from protruding luminal surfaces in many cases. Instead, longitudinal distances of lesions were calculated based on the number of frames when the external elastic membrane (EEM) was invisible.

For comparison, the depth, width, and area of each ablation lesion were measured in the corresponding histological sections with image analysis software (CellSens; Olympus, Tokyo, Japan) via a light microscope (BX53; Olympus).

2.4 | Statistical analysis

All data are presented as mean $\pm$ SD. Diameters of collagen fibrils in TEM images from ablation lesions and intact arterial adventitia were compared using Aspin–Welch t-tests following confirmation of the inhomogeneity of variance tested using the F test ($P < 0.05$). Pearson correlations were used in the comparison of dimensions in ablation lesions between histopathology and IVUS or OFDI. A P-value < 0.05 was considered statistically significant. Data were analyzed with EXSUS software (ver. 7.7.1; Arm Systex Co., Ltd., Osaka, Japan) in combination with SAS (ver. 9.2 TS2M3; SAS Institute Inc., Cary, NC, USA).

3 | RESULTS

3.1 | Histopathology in vivo ablation

When compared with the intact renal arteries, the ablated renal arterial wall showed prominent histopathological changes immediately after radiofrequency treatment; we consistently found medial coagulation, frequently with thinning (19 out of 21 ablation lesions in sections taken at 0.25-mm intervals; Figure 2a,b), and adventitial coagulation with thickening (Figure 2a,c). Endothelial cells on coagulated media were
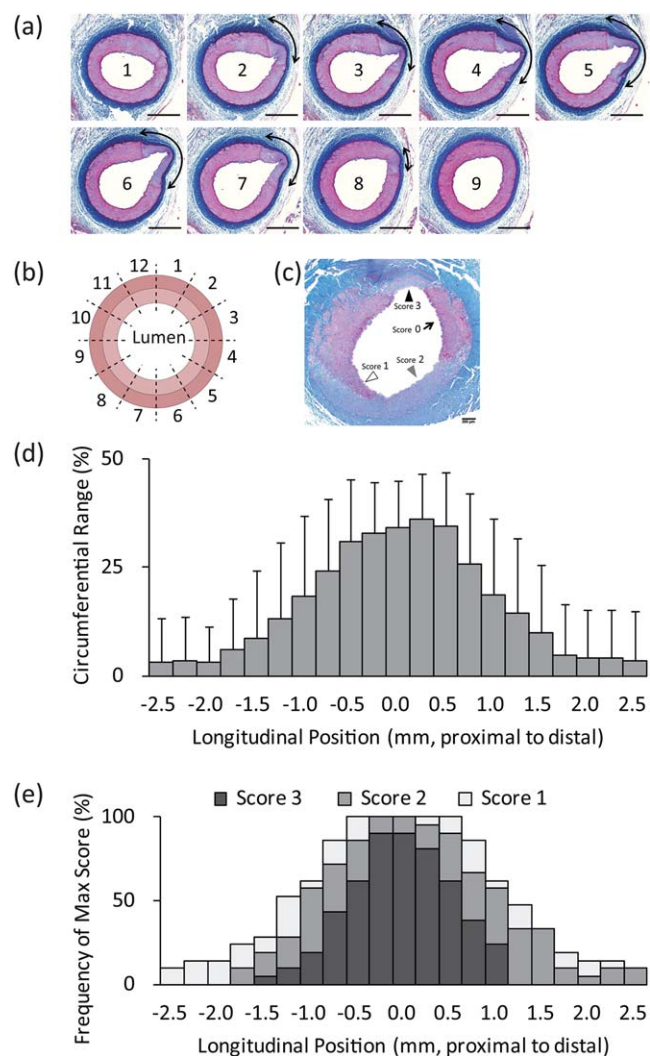
FIGURE 3 Representative images of serial arterial sections at 0.25-mm intervals. Circumferential range of medial changes (double arrows) peaked from the fourth to the sixth sections, and the highest score for medial change (score 3) was observed from the third to the sixth sections. Elastica Masson's trichrome staining. Scale bar = 1 mm (a). Illustration of divided areas (1–12 o'clock) (b). Examples of scoring in a Masson's trichrome-stained section. Scale bar = 200 μm (c). Distribution of circumferential range of medial changes (d). Distribution of maximum scores of medial changes. Cumulative bar at each longitudinal position represents the frequency of each score at the position (e) [Color figure can be viewed at wileyonlinelibrary.com]

almost completely denuded, while internal and external elastic lamina appeared intact.

Image analysis of ablated arteries sectioned at 0.25-mm intervals indicated that area (circumferential range) and severity of coagulated media had bell-shaped curves; the circumferential ranges were wider and scores for medial change were higher in the center of ablation lesions than in the periphery (Figure 3a,d,e).

In surrounding tissues, nerves and lymph nodes were affected when they were located in the vicinity of the coagulated adventitia. The affected nerve showed vacuolation and pyknosis (Figure 2d). In

affected lymph nodes, vacuolation of trabeculae and hemorrhage were found. No significant changes were noted in fat tissue.

3.2 | Histopathology and TEM in ex vivo ablation

In renal arteries ablated ex vivo, the same histopathological changes as seen in the in vivo study were observed. TEM revealed that adventitial collagen fibrils were swollen with obscure borders, loss of periodic striped pattern, and an increase in electron density, which are all signs of degeneration (Figure 4a). These degenerated changes were predominant in the center of ablation lesions compared with the border of the lesions. Quantitative analysis revealed that diameters in degenerated collagen fibrils were significantly larger than those in normal ones (233 ± 22 vs. 99 ± 11 nm; $P < 0.001$).

In TEM observations, medial smooth muscle cells in ablation lesions showed aggregation of nuclear chromatin, decreased myofilaments, and rich dense patches in cytoplasm (Figure 4b2,4c2). In medial smooth muscle cells in the intact arterial segment, the cytoplasm was almost filled with myofilament, suggesting that the dense patches in ablated media were aggregation of myofilament (Figure 4b,c). No change was found in external elastic lamina. In ablated unmyelinated nerve fibers, axons were dilated and axonal neurofilaments, microtubules, and intracellular organelles such as mitochondria were degenerated and decreased (Figure 4d). Similarly in myelinated nerve fibers, degeneration and decreased axonal neurofilaments, microtubules, and intracellular organelles were observed.

3.3 | Intravascular imaging in ex vivo ablation

In IVUS images at post-ablation, compared with those at preablation, regions bordered by the echogenic layer emerged in adventitia after ablation, while EEM remained distinguishable (Figure 5a). Intravascular OFDI images at post-ablation, compared with those at preablation, showed high scattering of signals in the surface layer and disappearance of EEM at ablated vessel walls (Figure 5b). Because of high signal attenuation, adventitia was almost invisible in ablation lesions, which precluded direct measurement of depth and area of ablation lesions (Figure 5b2). These changes in intravascular imaging were more prominent at the center of ablation lesions than at the periphery based on serial observations (Supporting Information Figure S2). The dimensions measured in intravascular imaging and histopathology showed good correlations (Figure 6). Although OFDI did not visualize deep layers in ablated adventitia, the diameters measured in OFDI images correlated with the depths of ablation lesions measured with histopathological examination (Figure 6e). Neither IVUS nor OFDI identified nerves at pre and post-ablation.

4 | DISCUSSION

To determine endpoints for success during RDN procedures, we detailed histopathological changes in renal arteries immediately after delivery of radiofrequency energy. This study is the first to indicate the feasibility of existing intravascular imaging systems at catheterization laboratories (IVUS and OFDI) to determine procedural success of RDN,
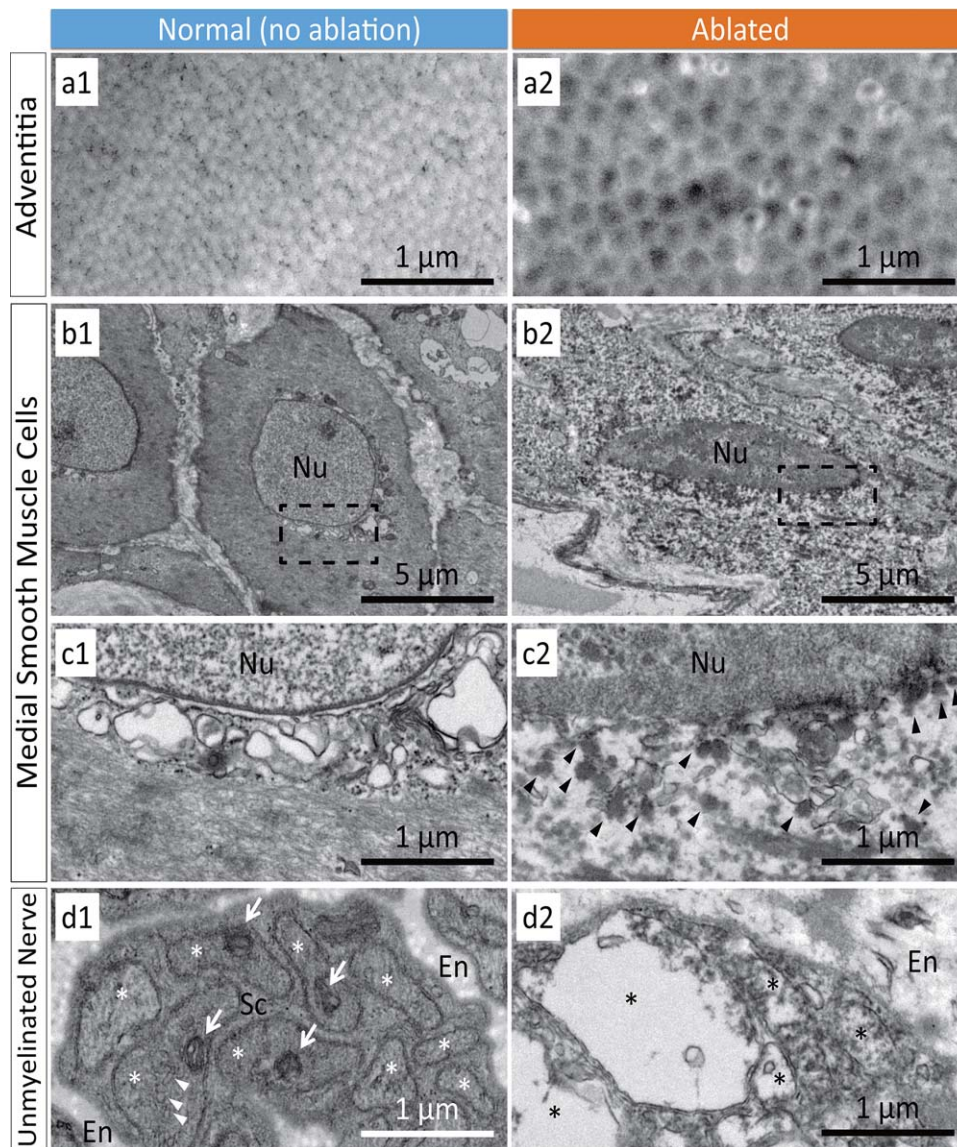
FIGURE 4 Representative TEM images. Cross sectional adventitial collagen fibrils in normal (a1) and at the center of the ablation lesion (a2). Thermally denatured collagen fibrils showed higher electron density and were swollen with indistinct outer borders in the ablation lesion (a2). Medial smooth muscle cells in normal (b1, c1) and at the center of the ablation lesion (b2, c2). Dotted boxes represent magnified positions of panel (c). Medial smooth muscle cells in ablation lesions showed aggregation of nuclear chromatin, decreased myofilaments, and rich, dense patches (arrowheads) in cytoplasm. Unmyelinated nerves in normal (d1) and at the center of the ablation lesion (d2). Axons (asterisks) were dilated and axonal neurofilaments, microtubules (arrowheads), and intracellular organelles such as mitochondria (arrows) were degenerated and decreased. Nu, nuclear; En, endoneurium; Sc, Schwann cell [Color figure can be viewed at wileyonlinelibrary.com]

since they were able to detect histopathological changes in ablated renal arteries, and dimensions of ablation lesions showed positive correlations between histopathology and IVUS/OFDI.

Despite the importance of revealing histopathological changes immediately after RDN, only Steigerwald et al. [14] have reported on acute changes. In the current study, we examined the acute changes in greater detail than the study by Steigerwald et al. using histopathological sectioning at 0.25-mm intervals and TEM. Prominent changes immediately after ablation were found in media, adventitia, and nerves. In particular, ablated adventitia was significantly thickened compared with normal adventitia. Ultrastructural

observations with TEM identified that each collagen fibril in the ablated adventitia was thickened.

Increases in the size of collagen fibrils by thermal denaturation has been reported in skin and tendons [15,16], and the mechanism is thought to be dissociation of the triple helix of collagen molecules [15]. As collagen fibers are abundant in adventitia of renal arteries, thermal denaturation of collagen molecules could have led to the thickening of the entire adventitia in this study.

Medial coagulation and thinning were also prominent changes. Sakakura et al. [9] reported that medial thinning was marked at 1 week after delivery of radiofrequency energy, when smooth muscle cells
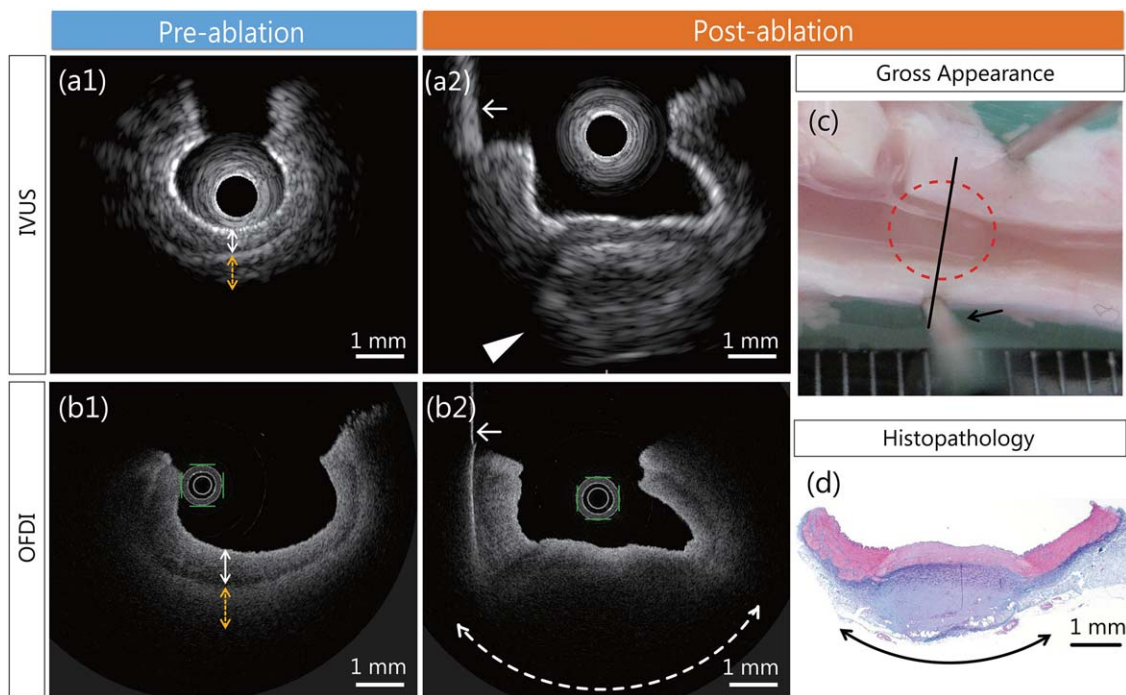
FIGURE 5 Representative images in ex vivo ablation. In IVUS, EEM was distinguishable as a clear border between media (solid white double arrow) and adventitia (dotted orange double arrow) at preablation (a1). At post-ablation (a2), EEM was still distinguishable but a mass bordered by an echogenic layer emerged in adventitia (white arrowhead). In OFDI, EEM was distinguishable as a clear border between media (solid white double arrow) and adventitia (dotted orange double arrow) at preablation (b1). At post-ablation (b2), EEM was invisible and more signals were attenuated in the arc from 4 to 8 o'clock (dotted white double arrow). In the gross image of the harvested renal artery (c), the dotted circle represents the ablation lesion and the solid line represents the corresponding position of the intravascular and histopathological images (a, b, and d). A corresponding histopathological image with elastica Masson's trichrome staining. The ablated area was characterized by coagulated media and swollen adventitia (black double arrow) (d) [Color figure can be viewed at wileyonlinelibrary.com]
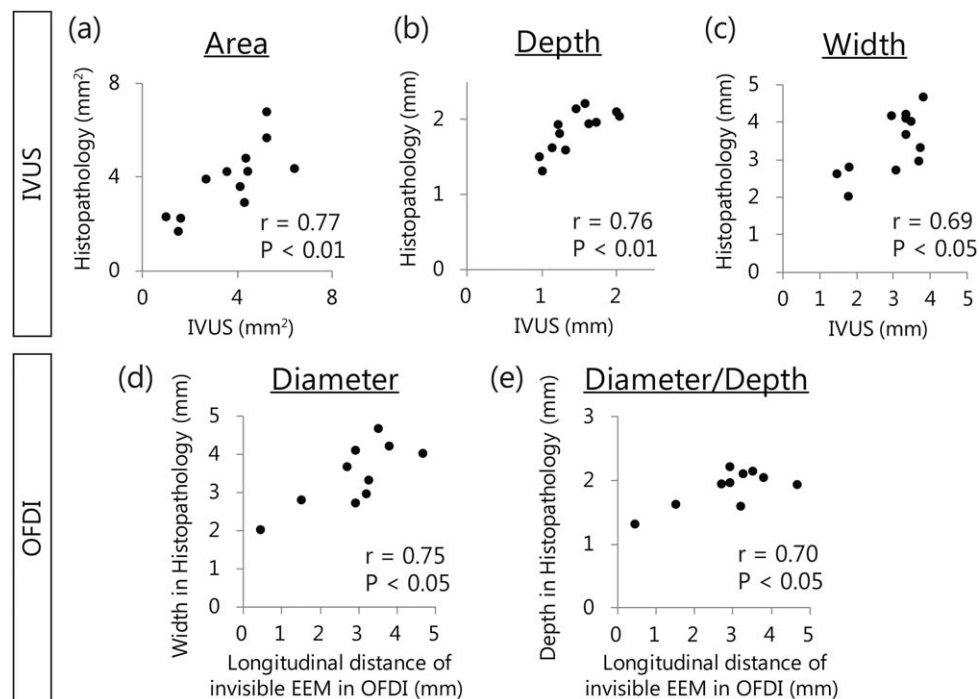

FIGURE 6 Scatter plots of dimensions of ablation lesions measured with intravascular imaging and histopathology. Pearson correlation coefficient (r) and P-values are shown in the plots. Adventitial areas (a), depths (b), and widths (c) measured with IVUS correlated to those measured with histopathology. Longitudinal distances of lesions measured with OFDI correlated to widths (d) and depths measured with histopathology (e). As ablated lesions appeared as circles on the luminal surface, the longitudinal distance was termed "diameter" and was regarded as the same as width

were lost. In the current study, we found that media thinned earlier, immediately after treatment, because of atrophy of medial smooth muscle cells. Nerve cell damage was observed, suggesting that denervation occurs immediately. No changes were noted in elastic fibers of the EEM or in fat tissue surrounding nerves, suggesting that they are less likely to be suitable targets for detection by imaging modalities immediately after treatment.

Angiographic luminal irregularity after RDN, which is known as "notch" in both clinical and animal studies [3,6,17,18], is suggested to be a sign of thickened media due to edema [19]. However, in the current study, edematous swollen media was neither confirmed with light microscopy nor TEM (increased area of low electron density). Instead, it was coagulated adventitia that was the most morphologically enlarged. Furthermore, a reduced myofilament density in ablated medial smooth muscle cells observed on TEM suggested loss of the contractile property of the cells. Given these results, this study suggests that angiographic notches are signs of thickened adventitia and/or inhomogeneous spasm responding to physical contact with intravascular devices.

To date, studies to observe renal arteries with intravascular imaging systems are mostly limited to morphological assessments of the luminal surface [18–22]. Here we focused on tissue characterization changes in deeper vessel layers. Based on the in vivo findings noted earlier, we hypothesized that changes in renal arteries and nerves were candidates for detection using intravascular imaging immediately after RDN. However, nerves were neither identified by IVUS nor OFDI. Then, as a surrogate indicator, we focused on visualizing changes in renal arteries, including the adventitia, where some nerves are located. We found that IVUS visualized ablation lesions extending outside the EEM, and revealed that the depths, widths, and areas of ablation lesions can be measured with IVUS.

With OFDI/OCT, the ex vivo ablation study revealed that signals were markedly scattered and attenuated in the surface layer of ablation lesions, resulting in invisible EEM. These qualitative findings in OFDI/OCT are consistent with previous animal and clinical studies [19,21], suggesting that our findings of intravascular imaging in ex vivo ablation would be reproduced in vivo. In addition, our study demonstrated a quantitative correlation between OFDI and histopathology.

The median depth of sympathetic nerves from the renal-arterial lumen is 2.44 mm in humans [23], which is equivalent to the maximum depth of histopathologically identified ablation lesions (2.22 mm) in this ex vivo ablation study. Although it has not been determined what quantity of renal sympathetic nerves needs to be ablated in clinical settings, effective sympathetic denervation was achieved in a porcine model when more than 50% of the peri-renal arterial nerves were damaged [24]. These findings suggest that IVUS directly visualizes and OFDI estimates tissue changes immediately after ablation at the depth necessary for effective denervation.

Ablation in all four anatomical quadrants (superior, inferior, anterior, and posterior directions) enhanced the efficacy of a reduction in blood pressure [6], and is recommended by expert consensus [7]. IVUS and OFDI visualize cross sectional vessel tissues from the lumen to outside the EEM, and would therefore indicate whether all four quadrants are ablated.

5 | STUDY LIMITATIONS

First, caution is needed before applying our findings to humans because renal arteries of healthy swine may be different to those of hypertensive humans. Nevertheless, porcine renal arteries are anatomically similar to humans and use of porcine models is widely accepted to assess RDN devices [9–11]. Second, our intravascular imaging was limited to an ex vivo ablation study. However, histopathological changes by in vivo ablation were reproduced in the ex vivo ablation study and therefore intravascular imaging results in the ex vivo ablation study could be reproducible in an in vivo ablation study. Our findings for OFDI align with previous in vivo studies [19,21]. Third, neither IVUS nor OFDI identified nerve damage directly in this study. The development of technology to detect nerve changes would produce a more direct and accurate diagnosis of procedural success during RDN.

6 | CONCLUSIONS

We determined acute histopathological changes immediately after delivery of radiofrequency energy to porcine renal arteries and demonstrated the diagnostic feasibility of procedural success in RDN with currently available intravascular imaging systems, IVUS and OFDI. It is suggested that observation of treated renal arteries by IVUS or OFDI immediately after RDN improves the success rate of RDN by determining if thermal denaturation reaches the adventitial zone in each ablation lesion and if the four anatomical quadrants are ablated in the vessel.

DISCLOSURES

Atsushi Sakaoka, Yuji Onimura, Hitomi Hagiwara, and Hisako Terao are employees of Terumo Corporation. The other authors have no commercial, proprietary, or financial interest in any products or companies described in this article.

REFERENCES

[1] James PA, Oparil S, Carter BL, Cushman WC, Dennison-Himmelfarb C, Handler J, Lackland DT, LeFevre ML, MacKenzie TD, Ogedegbe O, et al. 2014 evidence-based guideline for the management of high blood pressure in adults: report from the panel members appointed to the Eighth Joint National Committee (JNC 8). Jama 2014;311:507–520.

[2] Schlaich MP, Lambert E, Kaye DM, Krozowski Z, Campbell DJ, Lambert G, Hastings J, Aggarwal A, Esler MD. Sympathetic augmentation in hypertension: role of nerve firing, norepinephrine reuptake, and Angiotensin neuromodulation. Hypertension 2004;43:169–175.

[3] Bhatt DL, Kandzari DE, O'Neill WW, D'Agostino R, Flack JM, Katzen BT, Leon MB, Liu M, Mauri L, Negoita M, et al. A controlled trial of renal denervation for resistant hypertension. N Engl J Med 2014;370:1393–1401.

[4] Esler MD, Bohm M, Sievert H, Rump CL, Schmieder RE, Krum H, Mahfoud F, Schlaich MP. Catheter-based renal denervation for treatment of patients with treatment-resistant hypertension: 36 month results from the SYMPLICITY HTN-2 randomized clinical trial. Eur Heart J 2014;35:1752–1759.

[5] Krum H, Schlaich MP, Sobotka PA, Bohm M, Mahfoud F, Rocha-Singh K, Katholi R, Esler MD. Percutaneous renal denervation in patients with treatment-resistant hypertension: final 3-year report of the Symplicity HTN-1 study. Lancet 2014;383:622–629.

[6] Kandzari DE, Bhatt DL, Brar S, Devireddy CM, Esler M, Fahy M, Flack JM, Katzen BT, Lea J, Lee DP, et al. Predictors of blood pressure response in the SYMPLICITY HTN-3 trial. Eur Heart J 2015;36: 219–227.

[7] Mahfoud F, BM, Azizi M, Pathak A, Durand Zaleski I, Ewen S, Tsioufis K, Andersson B, Blankestijn PJ, Burnier M, et al. Proceedings from the European clinical consensus conference for renal denervation: considerations on future clinical trial design. Eur Heart J 2015; 36:2219–2227.

[8] Barrett CJ. Renal sympathetic nerves - what have they got to do with cardiovascular disease?. Exp Physiol 2015;100:359–365.

[9] Sakakura K, Tunev S, Yahagi K, O'Brien AJ, Ladich E, Kolodgie FD, Melder RJ, Joner M, Virmani R. Comparison of histopathologic analysis following renal sympathetic denervation over multiple time points. Circ Cardiovasc Interv 2015;8:e001813.

[10] Rousselle SD, Brants IK, Sakaoka A, Hubbard B, Jackson ND, Wicks JR, Dillon KN, Naiche LA, Hart R, Garza JA, et al. Neuromatous regeneration as a nerve response after catheter-based renal denervation therapy in a large animal model: immunohistochemical study. Circ Cardiovasc Interv 2015;8:e002293.

[11] Cohen-Mazor M, Mathur P, Stanley JR, Mendelsohn FO, Lee H, Baird R, Zani BG, Markham PM, Rocha-Singh K. Evaluation of renal nerve morphological changes and norepinephrine levels following treatment with novel bipolar radiofrequency delivery systems in a porcine model. J Hypertens 2014;32:1678–1691. discussion 1691–1692.

[12] Honton B, Pathak A, Sauguet A, Fajadet J. First report of transradial renal denervation with the dedicated radiofrequency Iberis catheter. EuroIntervention 2014;9:1385–1388.

[13] Jiang XJ, Dong H, Liang T, Zou YB, Xu B, Gao RL. First-in-man report of a novel dedicated radiofrequency catheter for renal denervation via the transulnar approach. EuroIntervention 2013;9:684–686.

[14] Steigerwald K, Titova A, Malle C, Kennerknecht E, Jilek C, Hausleiter J, Nährig JM, Laugwitz K-L, JONER M. Morphological assessment of renal arteries after radiofrequency catheter-based sympathetic denervation in a porcine model. J Hypertens 2012;30: 2230–2239. Volume p

[15] Lin M, Zhai X, Wang S, Wang Z, Xu F, Lu TJ. Influences of supra-physiological temperatures on microstructure and mechanical properties of skin tissue. Med Eng Phys 2012;34:1149–1156.

[16] Zelickson BD, Kist D, Bernstein E, Brown DB, Ksenzenko S, Burns J, Kilmer S, Mehregan D, Pope K. Histological and ultrastructural evaluation of the effects of a radiofrequency-based nonablative dermal remodeling device: a pilot study. Arch Dermatol 2004;140: 204–209.

[17] Hubbard B, Sakaoka A, Brants IK, Dillon KN, Brady DA, Rousselle SD, Devireddy CM, Mahfoud F, Tellez A. Sub-acute safety and efficacy evaluation of a single versus double treatment cycles of a monopolar radiofrequency catheter-based renal nerve ablation and its chronic evolution in a large animal model. J Adv Ther Med Innov Sci 2016;1:30–38.

[18] Templin C, Jaguszewski M, Ghadri JR, Sudano I, Gaehwiler R, Hellermann JP, Schoenenberger-Berzins R, Landmesser U, Erne P, Noll G, et al. Vascular lesions induced by renal nerve ablation as assessed by optical coherence tomography: pre- and post-procedural comparison with the Simplicity catheter system and the EnligHTN multi-electrode renal denervation catheter. Eur Heart J 2013;34:2141–2148. 2148b.

[19] Steigerwald K, Titova A, Malle C, Kennerknecht E, Jilek C, Hausleiter J, Nahrig JM, Laugwitz KL, Joner M. Morphological assessment of renal arteries after radiofrequency catheter-based sympathetic denervation in a porcine model. J Hypertens 2012;30: 2230–2239.

[20] Karanasos A, Van Mieghem N, Bergmann MW, Hartman E, Ligthart J, van der Heide E, Heeger CH, Ouhlous M, Zijlstra F, Regar E, et al. Multimodality Intra-arterial imaging assessment of the vascular trauma induced by balloon-based and nonballoon-based renal denervation systems. Circ Cardiovasc Interv 2015;8:e002474.

[21] Ierna S, Biondi-Zoccai G, Bachis C, Occhipinti M, Di Vito L, Ricciardi A, Pappone C, Prati F. Transcatheter renal sympathetic ablation for resistant hypertension: in vivo insights in humans from optical coherence tomography. Int J Cardiol 2013;165:e35–e37.

[22] Damascelli B, Patelli G, Ticha V, Della Rocca F, Lattuada S, Sala C, Albertoni A, D'Alessio A, Funaro A, Scotti L. Catheter-based radiofrequency renal sympathetic denervation for resistant hypertension. J Vasc Interv Radiol 2013;24:632–639.

[23] Sakakura K, Ladich E, Cheng Q, Otsuka F, Yahagi K, Fowler DR, Kolodgie FD, Virmani R, Joner M. Anatomic assessment of sympathetic peri-arterial renal nerves in man. J Am Coll Cardiol 2014;64: 635–643.

[24] Tzafriri AR, Mahfoud F, Keating JH, Markham PM, Spognardi A, Wong G, Fuimaono K, Bohm M, Edelman ER. Innervation patterns may limit response to endovascular renal denervation. J Am Coll Cardiol 2014;64:1079–1087.

SUPPORTING INFORMATION

Additional Supporting Information may be found in the online version of this article.